Sci. Bull.
DOI 10.1007/s11434-016-1092-0

www.scibull.com
www.springer.com/scp

Article

Engineering Sciences

Experimental and numerical investigation of a solar eductor-assisted low-pressure water desalination system

Mehran Ahmadi · Poovanna Thimmaiah · Majid Bahrami · Khaled Sedraoui · Hani H. Sait · Ned Djilali

Received: 19 March 2016 / Revised: 16 April 2016 / Accepted: 18 April 2016

Abstract Greenhouse solar-energy driven desalination technology is potentially well suited for supplying water and small scale irrigation in remote and/or rural areas, and for avoiding over-exploitation of available water resources. The efficiency and productivity of these systems are however low, in part because the heat of evaporation has to be transferred as waste heat to ambient air during condensation. In order to maximize energy regeneration during condensation we propose an educator based system that lowers the evaporation process temperature by reducing pressure. The feasibility of the educator assisted passive solar desalination system is investigated using a detailed computational fluid dynamics analysis complemented by experiments. The study focuses in particular on the ability of the new design to lower the required evaporation temperature and thereby reduce the energy intensity of the process. Two configurations, with open and closed educator, are investigated and a detailed analysis of the thermofluid processes is presented. The configuration with a closed educator installed outside the evaporation chamber shows very promising performance. The proposed system can maintain the maximum temperature and pressure in the evaporation chamber below the desirable temperature and pressure thresholds (30 °C and 5 kPa). The analysis and experimental data also show it is possible to further reduce energy requirements by reducing the motive water flow rates.

Keywords Desalination · Solar energy · Evaporation · Humidification · Dehumidification · Regenerative heating

1 Introduction

By 2050, global water demand is expected to rise by 55 % due to a combination of population and economic growth with more affluent lifestyles [1]. This will impose significant additional demands on already strained fresh water resources and could results in over 40 % of the world population living under water stressed conditions [1–3]. Water desalination has already seen significant growth in capacity in the last two decades and is widely seen as a key component of the future fresh water supply chain. Numerous desalination technologies have been developed and deployed: all require major infrastructure, long-term planning, proper maintenance, and most significantly, all are energy intensive. Consequently, there has been considerable interest in the development of water desalination using low carbon/renewable energy resources, and integrated solar desalination technologies in particular [4–6].

Typical concentration of dissolved salts in seawater and brackish water are 35,000 and 1,000 mg/L, respectively [7]. The two most widely used processes for water desalination are: (1) membrane separation processes including reverse osmosis (RO) and electro-dialysis (ED) [8]; and (2) thermal separation processes such as multistage

M. Ahmadi · P. Thimmaiah · M. Bahrami (✉)
Laboratory for Alternative Energy Conversion (LAEC), School of Mechatronic Systems Engineering, Simon Fraser University, Surrey, BC V3T 0A3, Canada
e-mail: mbahrami@sfu.ca

K. Sedraoui · H. H. Sait · N. Djilali
Renewable Energy Research Group, King Abdulaziz University, Jeddah, Saudi Arabia

N. Djilali
Department of Mechanical Engineering, and Institute for Integrated Energy Systems, University of Victoria, Victoria, BC V8P 5C2, Canada

Published online: 24 May 2016

flash distillation (MSF), multi-effect distillation (MED), and mechanical vapor compression (MVC) [9]. Among these, RO and MSF currently account for the bulk (90 %) of installed seawater desalination capacity worldwide. Alternative less energy intensive technologies have been demonstrated but have not been deployed commercially due to cost and salinity limitations. Some notable examples are capacitive deionization (CDI), membrane capacitive deionization (MCDI) [10], and centrifugal membrane separation [11].

The main factors in selecting the appropriate technology for a specific site are the total investment, operation/maintenance costs, availability of energy resources, and other parameters such as regional incentives and environmental impact [12, 13]. The cost of desalination with different processes is highly site-specific and depends on parameters including feed water salinity and other water quality parameters, plant capacity, energy and labor costs, political, and environmental restrictions. Table 1 compares the costs of water desalination for the principal desalination techniques.

The values in Table 1 indicate that the energy costs are slightly higher for thermal systems (MSF and MED) compared to RO plants, but it should be noted that RO technology loses its cost advantage when at smaller scales, where low capacity of water recovery and the inability to implement effective energy recovery techniques become major drawbacks. The major operational cost for RO is related to membrane maintenance and replacement, while for thermal systems it is the energy required for the water evaporation process. It is estimated that about 9.2 tonne of oil equivalent (107,000 MWh) is required per year to produce 1 m^3/d of fresh water by thermal desalination techniques [4]. When considering the cost and emissions associated with providing the required low grade thermal energy to drive thermal desalination, it is clear that this technology is much more viable if coupled effectively with renewable energy sources. Solar energy is a prime candidate and is typically highly available in arid locations where desalination is required [15]. Solar heat can either be used as the only source of thermal energy for thermal desalination processes [16–19], or in combination with other energy sources such as low grade thermal energy in hybrid systems [20–22]. Although combining renewable energy sources with established water desalination methods can decrease operational cost and increase efficiency, the implementation in available systems faces challenges including complexity, large footprint, and high maintenance. The design and development of simple and low-maintenance alternative water desalination technology integrated with sustainable energy sources and capable of working efficiently at small scales can fill niche markets of distributed local water desalination. This paper focuses on a novel design suitable for this purpose.

A particularly interesting semi-passive solar technology is the greenhouse solar desalination technology that exploits evaporation–condensation cycles [22–25]. The efficiency and productivity of these systems is however low, in part because the heat of evaporation, which is valuable energy, has to be transferred as waste heat to ambient air during condensation. In order to maximize the energy regeneration of the condensation process and minimize the capital cost alternative designs are required to achieve the optimum temperature difference between the solar-generated vapor and the seawater-cooled condenser.

One solution to address the energy-intensive nature of solar desalination systems, is to reduce the pressure of the evaporation process to decrease the evaporation temperature [25]. Currently, this is mainly accomplished by using a vacuum pump. But this has the drawbacks of parasitic energy consumption and higher maintenance requirements. In this paper we propose and investigate a novel configuration for a solar desalination system in which both energy use and the pressure of the evaporation process are reduced by using an educator.

Table 1 Average water desalination cost for a plant delivering 170,000 m^3/d of potable water and located in the Middle East (Persian Gulf Water). Adapted from Ref. [14]

Type of cost	MSF	MED	RO
Thermal energy (M$)	105	105	0
Electric power (M$)	92	76	114
Operation and maintenance (M$)	25	22	60
Plant investment (M$)	180	195	170
Total cost (M$)	402	398	344
Water cost ($/$m^3$)	0.52	0.52	0.45

2 Eductor assisted desalination: principle of operation and background

A schematic of the proposed system is shown in Fig. 1. The concept employs eductors to create a partial vacuum in the evaporation section, and to simultaneously draw the vapor from the evaporation chamber. Solar energy is used to provide the required heat for evaporation.

This water desalination system benefits from the fact that the evaporation occurs at partial vacuum condition, while condensation takes place under atmospheric condition: the enthalpy of evaporation at 4 kPa (saturation temperature 24.08 °C) and 101.32 kPa (saturation temperature 99.97 °C) are 2432.4 and 2256.5 kJ/kg,

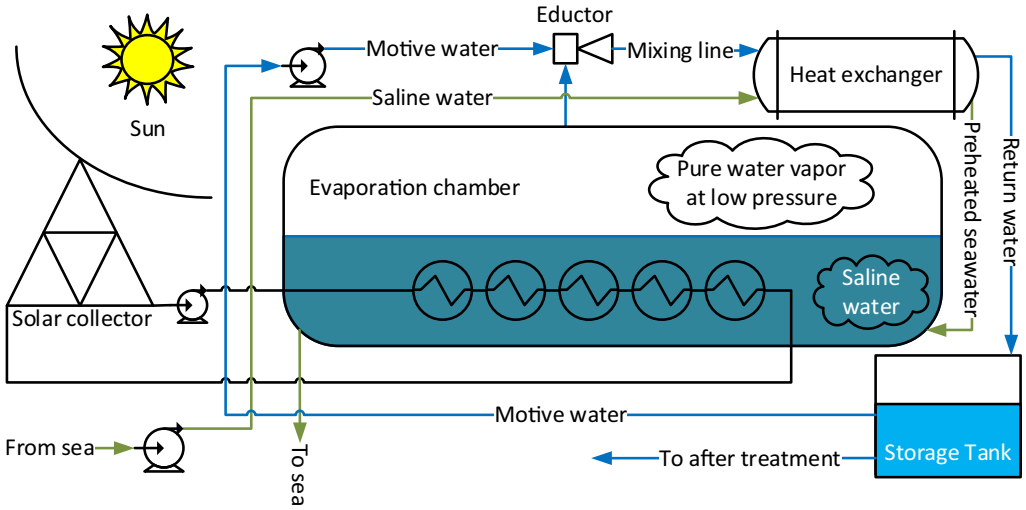

Fig. 1 (Color online) Schematic of solar eductor-assisted low-pressure water desalination

respectively. Although the thermal energy required for evaporation is slightly higher at lower pressure, the lower saturated temperatures make it possible to use "low-grade" heat to drive evaporation in partial vacuum. Furthermore, replacing the vacuum pump with eductor pumps will drastically decrease the energy consumption of the system as well as maintenance requirements.

Eductor pumps have been used in different industries since 1858 [26], and they rely on the classical Venturi effect in converging–diverging channels whereby the fluid flow is accelerated and the pressure reduced (suction) at the throat [27]. After passing through the throat of the injector, the mixed fluid expands and the velocity is reduced, resulting in recompression of the mixed fluids [28]. Eductor pumps have been the subject of research for a range of applications including geothermal energy, breweries, sugar refineries, and air conditioning [29–32]. They have also been investigated for their potential in water desalination systems, including solar-assisted vacuum freezing ejector absorption (VFEA) desalination plant [33] and steam-ejector refrigeration plants [34] which were shown to require less energy when steam ejectors were used to assist the heat recovery in the vapor compression systems. The case for exploiting low grade heat sources in desalination was made by Li in his thesis [35], and he proposed two cogeneration systems, one coupled to RO and the second to MED in conjunction with a Supercritical Organic Rankine Cycle (SORC) and an Ejector. Li's analysis showed the MED system operating with low grade heat at 150 °C could treat highly concentrated brine with no external power input, and could also operate in cogeneration mode to produce water and power simultaneously when not processing concentrated brine.

To the best of our knowledge, there have been no studies on the use of eductors for the type of low-pressure solar water desalination system shown in Fig. 1. An eductor (Fig. 2), is essentially a jet-pump that typically consist of a nozzle through which the primary (motive) fluid, in this case water, is injected into a chamber containing a

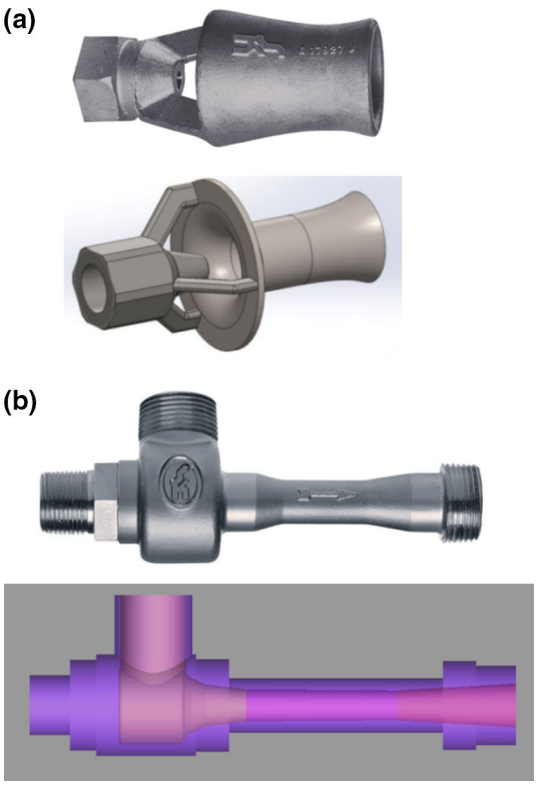

Fig. 2 (Color online) Schematic and real picture of different types eductors used in the study: **a** open educator, **b** closed educator

secondary fluid (here water vapour). The primary fluid creates a low pressure zone region as it exits the nozzle and sucks (entrains) the secondary fluid. As the two fluids proceed downstream into the converging section, they mix and accelerate and their pressure drops attaining a minimum at the throat of the converging–diverging section (see e.g. Ref. [29] for a more detailed description of operating principle). In the proposed system, the eductor which is fed by motive water is used to maintain the required low pressure and pump the water vapor from the evaporation chamber. Water vapor condensation occurs mainly inside the mixing line and also inside the storage tank.

A number of parameters affect the overall performance of the proposed system, including: the motive water flow rate, nozzle geometry, converging–diverging section geometry, type of eductor, location of eductor, and size of evaporation chamber. In addition, the motive water temperature and the evaporation chamber pressure play a determining role on the condensation process and the overall energy efficiency of the system. To provide a detailed understanding of the system operation, a comprehensive numerical study is conducted and complemented by an experimental investigation. The primary focus of this study is on the evaporation chamber and eductor pump, thus in the numerical and experimental studies, the solar collectors, water storage tank, and heat exchangers, are not explicitly included, and are considered off-the-shelf items. Two different types of eductors, open and closed, are used for this study (Fig. 2). Open eductors are mainly used for mixing purposes, requiring installation inside the evaporation chamber, while closed eductors can be installed outside the chamber. Numerical simulations are first presented in the next section to analyze in details the thermo-fluid transport, the eductors effectiveness and water removal capacity of each of the two eductor configurations. This is followed by a presentation of a test bed assembled as a proof of concept and instrumented to provide data on key thermodynamic and energy performance parameters.

3 Numerical study

In order to analyze the process in detail and guide the design, a 3D CFD model is developed in this section, using ANSYS Fluent. The simulations are performed to model the 3-foot long (1 foot = 30.48 cm), 1-foot diameter evaporation chamber with one eductor as shown in Fig. 3. The sizing and base operating parameters of eductors are obtained from manufacturer (Schutte & Koerting) specs (Figs. 4, 5).

Steady state operation is considered. The high flow velocities in the educator result in a Reynolds number of order 10^5, i.e. much larger than the critical transition value (2.3×10^3), and the flow is thus considered fully turbulent. The convective and diffusive thermofluid transport processes are governed by the incompressible Navier–Stokes equations and the Energy equation in conjunction with the k–ε turbulence model, a multiphase mixture transport model, and source terms for the condensation/evaporation process. The conservation equations are solved with mass

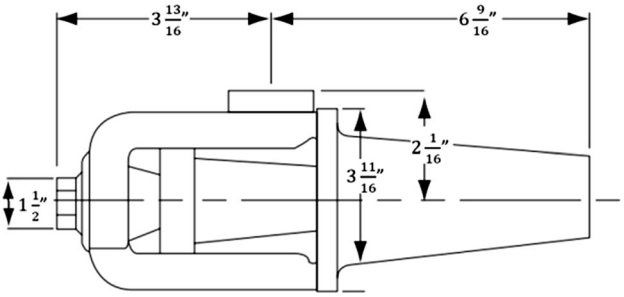

Fig. 4 Dimensions of open eductor (adapted from Schutte & Koerting datasheet)

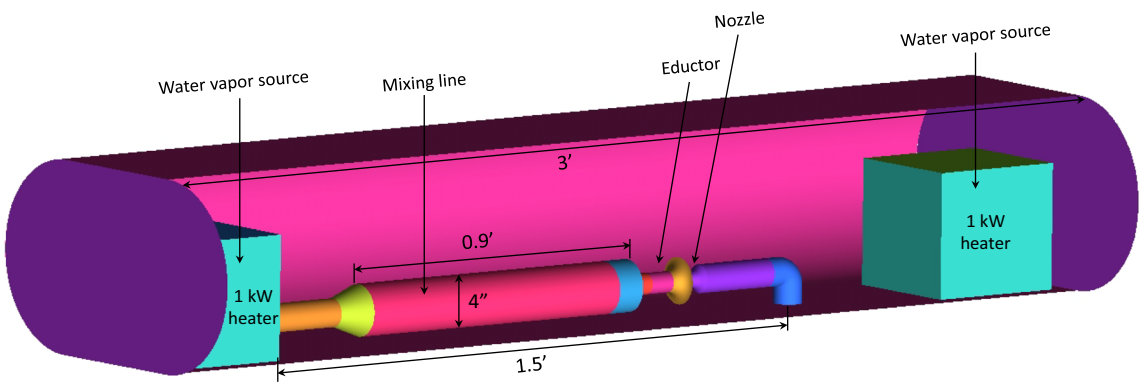

Fig. 3 (Color online) 3D geometry of the full scale evaporation chamber with transparent front side to show the heaters and open eductor, and dimensions of the main components

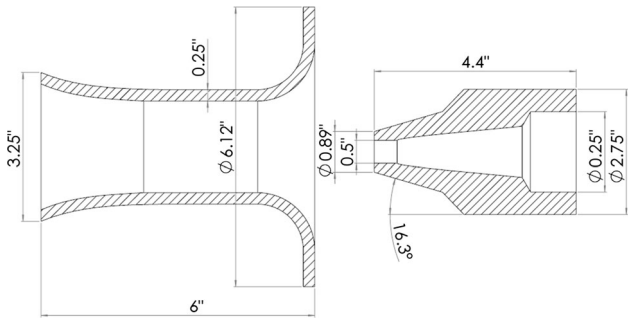

Fig. 5 Cross-section and dimensions of the open eductor

interaction model accounting for the phase interaction between water vapor and liquid. The governing equations detailed below are discretized using a second-order upwind scheme and solved with the SIMPLE algorithm.

3.1 Governing equations

3.1.1 Continuity equation

The continuity equation for the mixture is

$$\frac{\partial}{\partial t}(\rho_{\mathrm{m}}) + \nabla \cdot \left(\rho_{\mathrm{m}} \overrightarrow{v_{\mathrm{m}}}\right) = 0, \tag{1}$$

where the subscript "m" represents the mixture properties and v_{m} is the mass-averaged velocity and it can be obtained from

$$\overrightarrow{v_{\mathrm{m}}} = \frac{\sum_{i=1}^{n} \alpha_i \rho_i \overrightarrow{v_i}}{\rho_{\mathrm{m}}}, \tag{2}$$

where ρ_{m} is the mixture density

$$\rho_{\mathrm{m}} = \sum_{i=1}^{n} \alpha_i \rho_i, \tag{3}$$

and α_i is the volume fraction of phase i.

3.1.2 Momentum equation

The momentum equation for the mixture can be obtained by summing the individual momentum equations for all phases. It can be expressed as

$$\begin{aligned}\frac{\partial}{\partial t}\left(\rho_{\mathrm{m}} \overrightarrow{v_{\mathrm{m}}}\right) + \nabla \cdot \left(\rho_{\mathrm{m}} \overrightarrow{v_{\mathrm{m}}} \overrightarrow{v_{\mathrm{m}}}\right) &= -\nabla p + \nabla \cdot \left[\mu_{\mathrm{m}}\left(\nabla \overrightarrow{v_{\mathrm{m}}} + \nabla \overrightarrow{v_{\mathrm{m}}^{\mathrm{T}}}\right)\right] + \rho_{\mathrm{m}} \overrightarrow{g} + \overrightarrow{F} \\ &+ \nabla \cdot \left(\sum_{i=1}^{n} \alpha_i \rho_i \overrightarrow{v_{\mathrm{dr},i}} \overrightarrow{v_{\mathrm{dr},i}}\right),\end{aligned} \tag{4}$$

where n is the number of phases, F is a body force, and μ_{m} is the viscosity of the mixture,

$$\mu_{\mathrm{m}} = \sum_{i=1}^{n} \alpha_i \mu_i, \tag{5}$$

and $v_{\mathrm{dr},i}$ is the drift velocity for secondary phase i,

$$\overrightarrow{v_{\mathrm{dr},i}} = \overrightarrow{v_i} - \overrightarrow{v_{\mathrm{m}}}. \tag{6}$$

The relative velocity, also referred to as the slip velocity, is defined as the velocity of a secondary phase, s, relative to the velocity of the primary phase, l

$$\overrightarrow{v_{sl}} = \overrightarrow{v_s} - \overrightarrow{v_l}. \tag{7}$$

The mass fraction for any phase i, is defined as

$$c_i = \frac{\alpha_i \rho_i}{\rho_{\mathrm{m}}}. \tag{8}$$

The drift velocity and the relative velocity are connected by the following expression

$$\overrightarrow{v_{\mathrm{dr},s}} = \overrightarrow{v_{sl}} - \sum_{i=1}^{n} c_i \overrightarrow{v_{li}}. \tag{9}$$

The mixture model uses an algebraic slip formulation. The basic assumption of the algebraic slip mixture model is that to prescribe an algebraic relation for the relative velocity, a local equilibrium between the phases should be reached over short spatial length scale. Following Manninen et al. [36], the form of the relative velocity is given by

$$\overrightarrow{v_{sl}} = \frac{\tau_s}{f_{\mathrm{drag}}} \frac{(\rho_s - \rho_{\mathrm{m}})}{\rho_l} \overrightarrow{a}, \tag{10}$$

where τ_s is the particle relaxation time

$$\tau_s = \frac{\rho_s d_s^2}{18 \mu_l}, \tag{11}$$

d is the diameter of the particles of secondary phase s, a is the secondary-phase particle's acceleration. The default drag function f_{drag} is taken from Schiller and Naumann [37]:

$$f_{\mathrm{drag}} = 1 + 0.15\mathrm{Re}^{0.687}, \quad \text{if} \quad \mathrm{Re} \leq 1{,}000, \tag{12}$$

$$f_{\mathrm{drag}} = 0.0183\mathrm{Re}, \quad \text{if} \quad \mathrm{Re} > 1{,}000, \tag{13}$$

and the acceleration a is of the form

$$\overrightarrow{a} = \overrightarrow{g} - \left(\overrightarrow{v_{\mathrm{m}}} \cdot \nabla\right) \overrightarrow{v_{\mathrm{m}}} - \frac{\partial \overrightarrow{v_{\mathrm{m}}}}{\partial t}. \tag{14}$$

In turbulent flows, the relative velocity should contain a diffusion term due to the dispersion appearing in the momentum equation for the dispersed phase. This dispersion to the relative velocity is added by

$$\overrightarrow{v_{sl}} = \frac{(\rho_s - \rho_{\mathrm{m}})}{18 \mu_l f_{\mathrm{drag}}} \overrightarrow{a} - \frac{v_{\mathrm{m}}}{\alpha_s \sigma_{\mathrm{D}}} \nabla \alpha_l, \tag{15}$$

where v_m is the mixture turbulent viscosity and σ_D is a Prandtl dispersion coefficient.

A wide array of models are available to account for turbulence, ranging from large-eddy simulation (LES) to simple algebraic models (see e.g. review in Ref. [38]). While LES is the most physical and comprehensive turbulence modelling approach, its high spatial and temporal resolution requirements restrict its practical application to relatively small flow systems/domains (e.g. Ref. [39]). The complex geometry, large domain and multi-phase flow effects in the solar desalination system considered here require the use of a robust CFD modeling approach to ensure convergence. The k–ε turbulence model was selected as it provides a reasonable compromise between computational cost and accuracy for the purpose of the present analysis which is primarily aimed at a design assessment. The standard k–ε turbulent accounts for turbulence in the momentum equations by using a turbulent (eddy) viscosity determined from the turbulence kinetic energy, k, and its rate of dissipation, ε, obtained by solving the following transport equations:

$$\frac{\partial}{\partial t}(\rho k)+\frac{\partial}{\partial x_i}(\rho k v_i)=\frac{\partial}{\partial x_i}\left[\left(\mu+\frac{\mu_t}{\sigma_k}\right)\frac{\partial k}{\partial x_i}\right]+G_k+G_b-\rho\varepsilon-Y_M+S_k, \tag{16}$$

$$\frac{\partial}{\partial t}(\rho \varepsilon)+\frac{\partial}{\partial x_i}(\rho \varepsilon v_i)=\frac{\partial}{\partial x_i}\left[\left(\mu+\frac{\mu_t}{\sigma_\varepsilon}\right)\frac{\partial \varepsilon}{\partial x_i}\right]+C_{1\varepsilon}\frac{\varepsilon}{k}(G_k+C_{3\varepsilon}G_b)-C_{2\varepsilon}\rho\frac{\varepsilon^2}{k}+S_\varepsilon, \tag{17}$$

where G_k represents the generation of turbulence kinetic energy due to the mean velocity gradients, G_b is the generation of turbulence kinetic energy due to buoyancy, Y_M represents the contribution of the fluctuating dilatation in compressible turbulence to the overall dissipation rate, $C_{1\varepsilon}$, $C_{2\varepsilon}$, and $C_{3\varepsilon}$ are constants, σ_k and σ_ε are the turbulent Prandtl numbers for k and ε, respectively, and S_k and S_ε are user-defined source terms.

3.1.3 Energy equation

The energy equation for the mixture takes the following form:

$$\frac{\partial}{\partial t}\sum_{i=1}^{n}(\alpha_i\rho_i E_i)+\nabla\cdot\sum_{i=1}^{n}\left[\alpha_i\overrightarrow{v_i}(\rho_i E_i+p)\right]=\nabla\cdot(k_{\text{eff}}\nabla T)+S_E, \tag{18}$$

where k_{eff} is the effective thermal conductivity, S_E includes any other volumetric heat sources, and

$$E_i=h_i-\frac{p}{\rho_i}+\frac{v_i^2}{2}, \tag{19}$$

for the compressible phase, and $E_i=h_i$ for the incompressible phase. The term h_i is the sensible enthalpy for phase i.

3.1.4 Volume fraction equation for the secondary phase

Lee's model [40] is used for interphase mass transfer through evaporation–condensation in the mixture. The volume fraction equation for secondary phase, s, can be obtained

$$\frac{\partial}{\partial t}(\alpha_s\rho_s)+\nabla\cdot\left(\alpha_s\rho_s\overrightarrow{v_m}\right)=-\nabla\cdot\left(\alpha_s\rho_s\overrightarrow{v_{dr,p}}\right)+\dot{m}_{ls}-\dot{m}_{sl}, \tag{20}$$

where $\dot{m}_{ls}$ and $\dot{m}_{sl}$ are the rates of mass transfer due to evaporation and condensation, respectively, and they can be described as

$$\dot{m}_{ls}=\omega\alpha_l\rho_l\frac{T_l-T_{\text{sat}}}{T_{\text{sat}}},\quad \text{if}\quad T_l>T_{\text{sat}}\ (\text{evaporation}), \tag{21}$$

$$\dot{m}_{sl}=\omega\alpha_s\rho_s\frac{T_{\text{sat}}-T_s}{T_{\text{sat}}},\quad \text{if}\quad T_s<T_{\text{sat}}\ (\text{condensation}). \tag{22}$$

The parameter ω is a coefficient that must be fine-tuned and can be interpreted as a relaxation time. The source term for the energy equation can be obtained by multiplying the rate of mass transfer by the latent heat.

3.2 3D CFD simulations with open eductor

The simulations are performed to model the 3-foot long, 1-foot diameter evaporation chamber with one eductor. The size of the evaporation chamber is selected to match the size of the chamber used in the experimental setup. The sizing and base operating parameters of the eductors are obtained from the selected manufacturer specs (Schutte & Koerting). Figure 4 shows the dimension of the open eductor used for the numerical simulations. The dimensions of the exit nozzle and the venturi section of the open eductor are also shown in Fig. 5.

3.2.1 Geometry and boundary conditions

The geometry consist of a 1.5-in. (1 in. = 2.54 cm) open eductor, located inside a 3-foot long evaporation chamber and connected to a 4-in. mixing line through an adaptor, as shown in Fig. 3. The mixing line length is assumed to be 0.9-foot. Two steam generators are placed at both ends of the evaporation chamber. Each steam generator is driven by a 1 kW electric heater. Mass flow boundary conditions are set for the water vapor sources at the steam generators. The motive fluid mass flow rate and temperature are

prescribed at the inlet of the eductor's nozzle, and atmospheric pressure is prescribed at the mixing line outlet. Table 2 lists the boundary conditions used for 3D numerical simulations.

3.2.2 *Mesh generation*

The computational domain is large and relatively complex, but computational costs are reduced by taking advantage of symmetry (Fig. 6a). This only half of the geometry is considered. Figure 6b shows the simplified geometry model with the associated structured grid.

Table 2 Boundary conditions used in the 3D numerical simulations

Parameter	Value
Heater input power	0.1 (kW)
Vapor saturation temperature	22.2 (°C)
Vapor mass flow rate	0.38 (g/s)
Motive water temperature	17 (°C)
Motive water flow rate	27 (gpm) $\approx$ 6.12 (m^3/h)
Mixing line outlet pressure	101.325 (kPa)

The computational mesh consists of approximately 3 million hexahedral elements with 2.9 million nodes. The CFD simulations are performed on 3 PCs with Windows 8.1 64-bit operating system, 64×-based Intel Core i7 processors and 32 GB RAM. Each simulation requires around 180 h of clock time to achieve a converged flow field.

To assess uncertainties due to numerical discretization, a grid sensitivity study is performed for the open eductor case, and error estimates were performed following the systematic procedure of Celik et al. [41]. The vapor pressure inside the evaporation chamber at the entrance of educator, a key parameter for the performance of the design, is selected as a monitoring parameter and shown in Fig. 7 for three grids. The results show that for 3 million computational cells, there is a relative difference of approximately 12 % compared to the case with roughly 1.5 million cells. Using the Grid Convergence Method [39] based on Richardson extrapolation, the estimated discretization error for the finest 3 million cells grid is ±7.5 %. This grid was used for all calculations.

Figure 8 shows the predicted velocity, pressure, and vapor volume fraction contours inside the evaporation chamber. Although a mixture plume forms inside the

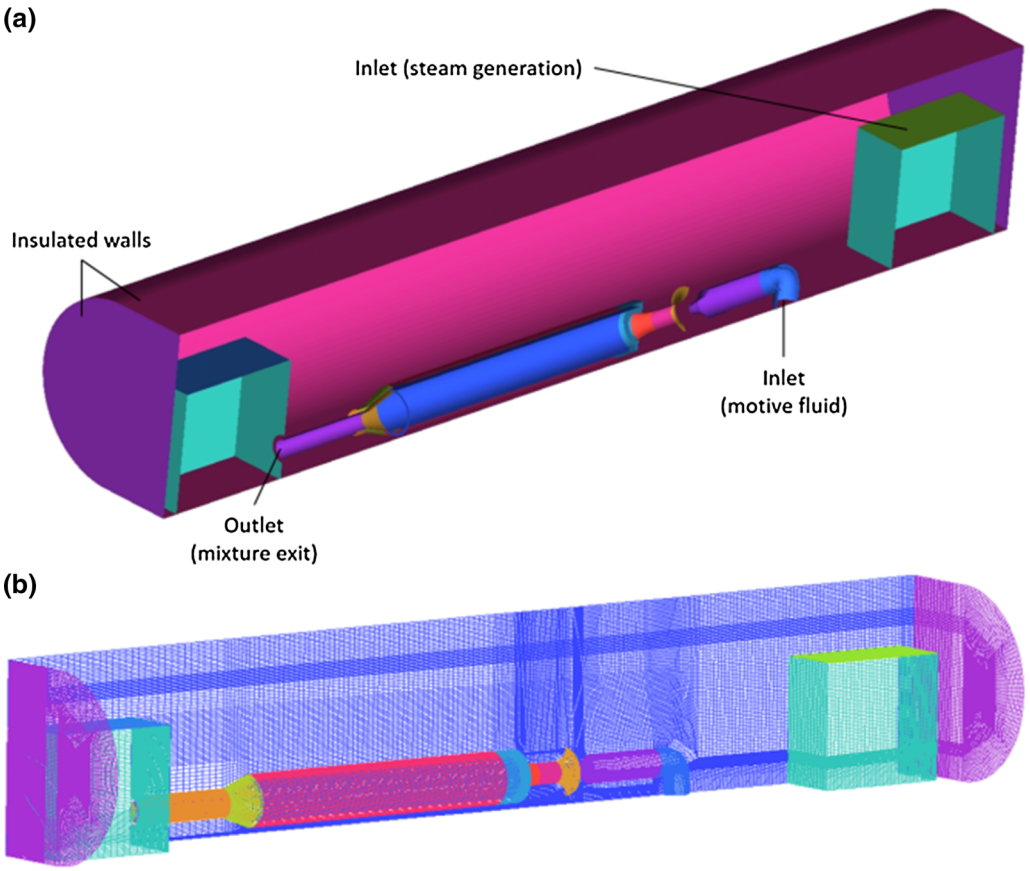

Fig. 6 (Color online) **a** Half geometry used for numerical simulations due to symmetry, **b** structured mesh generated using hexahedral elements

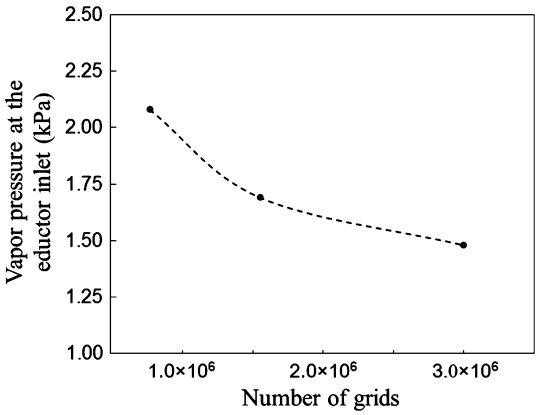

Fig. 7 Grid sensitivity study for the open eductor

mixing line, it is relatively short because of the sudden expansion inside the mixing line and the 2-in. ID outlet pipe. The pressure inside the evaporation chamber is shown in Fig. 8b and remains at more than 10 kPa which is not desirable for a low pressure evaporation process. The "in-chamber" open inductor arrangement offers economic advantages as it does not require any additional mounting structures outside the chamber, and it can rely on the use of existing transfer pumps. However the predicted vapor volume fraction distribution inside the system in Fig. 8c indicates this open eductor is not capable of condensing the mixture sufficiently in the mixing line. Consequently, an analysis was performed to investigate the performance of the alternative closed eductor arrangement presented next.

3.2.3 3D CFD simulations with closed eductor

In this section, a 1.5-in. closed eductor (Fig. 9), installed outside the 3-foot long and 1-foot diameter evaporation chamber, is modeled. The complete assembly considered in the numerical model is shown in Fig. 10a. As mentioned before, to reduce the computational cost and due the symmetry, half of the domain is used for the numerical simulations (Fig. 10b). The structured mesh generated using ICEM CFD is shown in Fig. 10c. The mesh consists of approximately 2.6 million hexahedral elements with 2.4 million nodes. Prescribed velocity inlet and pressure outlet boundary conditions are used for the eductor inlet and mixing line outlet respectively. Mass flow inlet boundary condition is assumed for water vapor sources located at the two ends of the evaporation chamber. Table 2 shows the boundary conditions used in the simulations. Due to the complex geometry at the eductor inlet, a good quality structured mesh could not be generated in this region, and an unstructured tetrahedral mesh is used instead (Fig. 10b). Grid independence study and careful inspection of the flow field and mesh near the entrance to the eductor was performed to ensure appropriate resolution. Each simulation takes around 240 h to converge.

Figure 11 shows sample results obtained from the numerical simulations of the closed eductor. The mixture temperature (Fig. 11a) at the end of the mixing line is about 18 °C, which indicates the ability of the eductor-assisted system to condense the vapor generated in the evaporation chamber. This is confirmed by the vapor volume fraction distribution depicted in Fig. 11b and showing that more than 80 % of the vapor is condensed in the mixing line.

4 Experimental study

A testbed was designed and built to verify the results obtained from the numerical simulations. A 3-foot long cylindrical evaporation chamber, with a 1-foot cross section diameter is used to hold a water tank is located on top of the evaporation chamber to continuously provide the required water for evaporation. Motive water at 4–5 °C is pumped to the eductor. The testbed is also equipped with a 24-kW electric heater as a water vapor generator to mimic the chamber behavior under real operating conditions. To measure temperature, 10 type-J thermocouples provided by Omega are used. Three vacuum pressure transducers, with a range of 0–30 kPa and accuracy of 0.5 kPa are installed on the evaporation chamber. A pressure transducer with range of 0–5 bar is also installed on the motive water line. To measure the flow rates, two flow meters are installed on the motive water line and evaporation system water and evaporation system feed water line. Figure 12a shows a schematic of the testbed. A picture of the testbed with open eductor is also shown in Fig. 12b.

The experiments are conducted under the same conditions presented in Table 2. Each experiment is repeated twice to ensure the reproducibility of the data. No major difference (<4 % relative difference) is observed and the reported data are the average values of the measurements. Since the closed eductor showed more promising performance, only experimental results from the closed eductor testbed are presented. The temperature data from the experiment are monitored at the locations shown in Fig. 12a. Type-J thermocouples provided by Omega with accuracy of ±2.2 °C are installed at these locations. The temperature data from the CFD simulation are compared to experimental data for T_1, T_2 and T_3 (evaporation chamber temperature) in Fig. 13. It should be noted that the error bars presented in Figs. 13 and 14, are related to the accuracy of type-J thermocouples. Since the reported values are related to the measurement of one parameter only, no uncertainty analysis is conducted for the reported error bars. The predicted temperatures are in good agreement

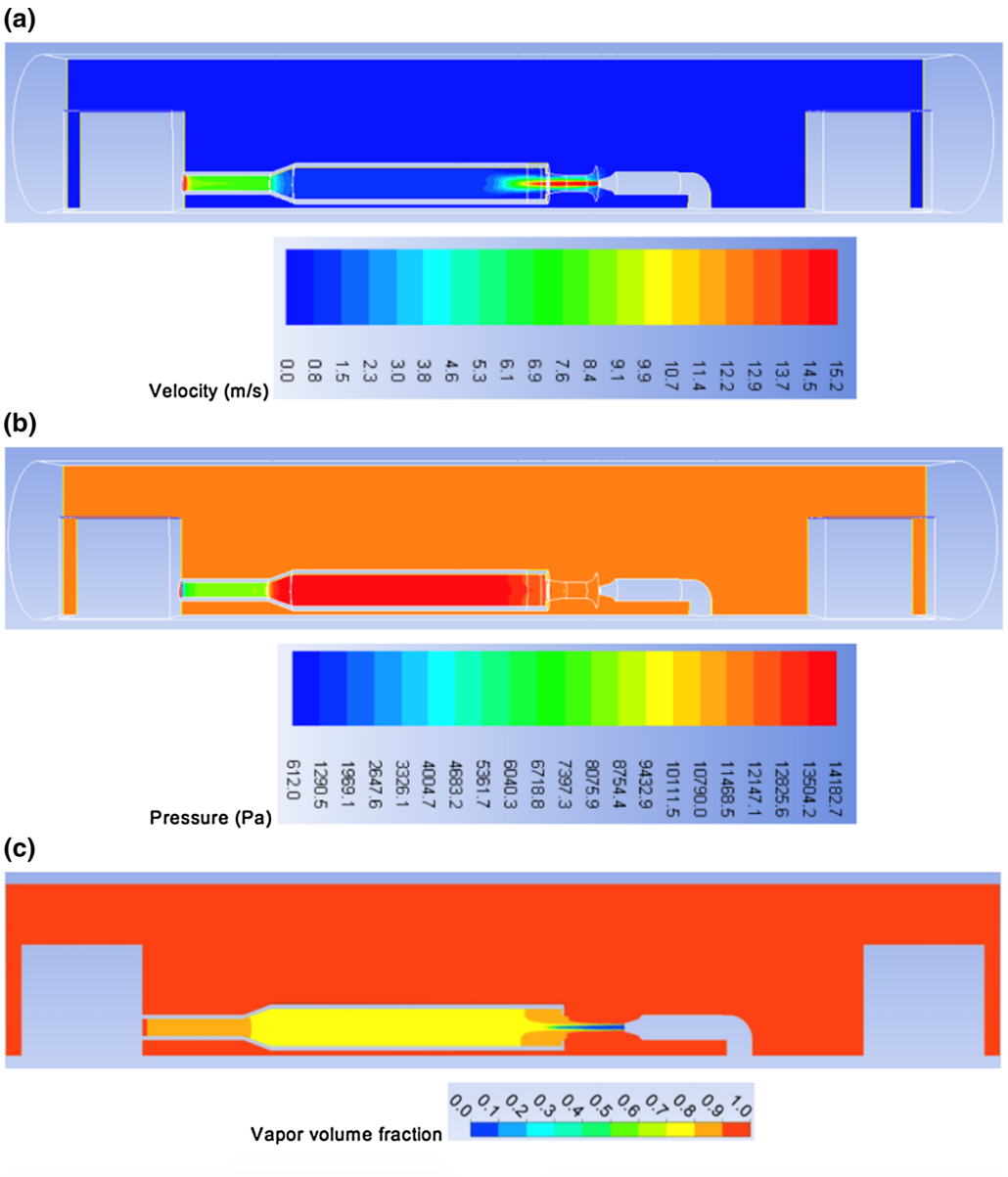

Fig. 8 (Color online) **a** Velocity, **b** pressure, and **c** vapor volume fraction contours inside the evaporation chamber with open eductor and 4-in. ID mixing line

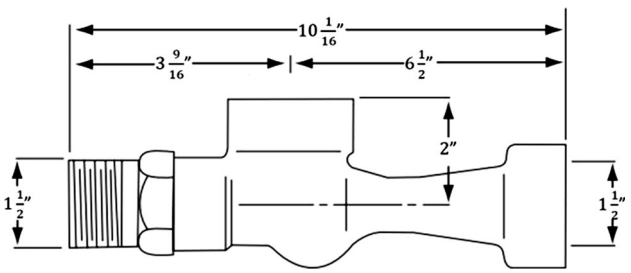

Fig. 9 Dimensions of closed eductor (adapted from Schutte & Koerting datasheet)

and with the measured values within the uncertainty limits of the thermocouple data, with the largest difference (1.7 °C) at location 3.

Figure 14 shows a comparison between the numerical simulations and experimental data for water vapor temperature at the eductor inlet and liquid water mixture temperature at the mixing line outlet, measured by thermocouples T_4 and T_5 respectively.

Table 3 summarizes the experimental and numerical data. Overall, the numerical simulation predicts the temperatures at different locations of the evaporation chamber

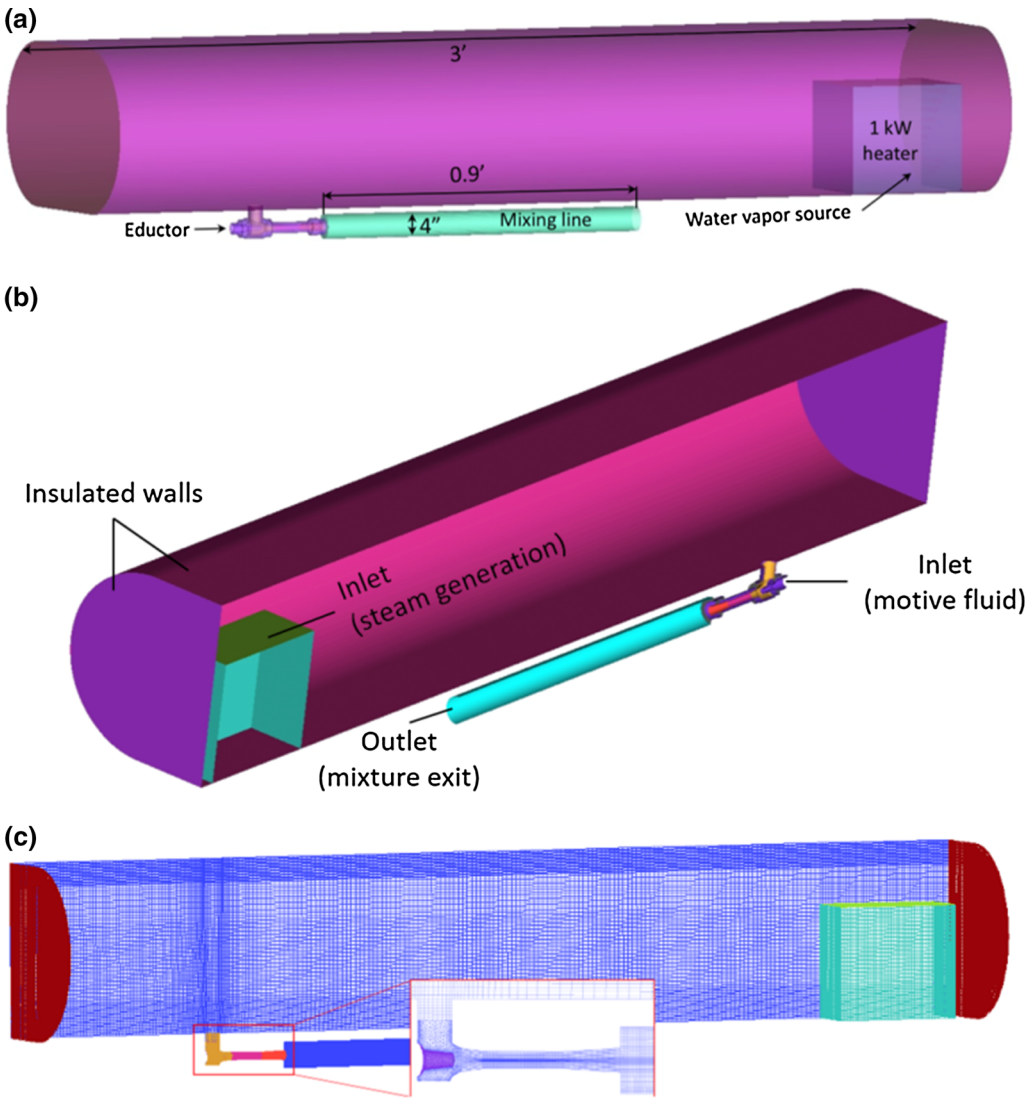

Fig. 10 (Color online) **a** Schematic of the evaporation chamber, eductor and mixing line with closed eductor, **b** half geometry used for numerical simulations due to symmetry, and **c** computational domain and mesh used for the CFD simulation

with satisfactory accuracy indicating their suitability for the design and performance analysis of the proposed water desalination system. The pressure of the evaporation chamber measured by a pressure transducer is (2.2 ± 0.4) kPa and the value calculated by the CFD simulation is 3.2 kPa.

To study the effects of water vapor generation rate on the temperature and pressure of the evaporation chamber, the motive water temperature and flow rate are kept constant at 4.3 °C and 178 gpm respectively, and different heating powers of 0, 7.7, 15.2 and 22.1 kW are imposed to the system by electrical heaters. Figure 15 shows the chamber temperature and pressure against different heating power inputs to the heaters. The chamber temperature and pressure increase from 13.7 °C and 1.36 kPa at zero heating power, to 25.9 °C and 2.71 kPa at 22.1 kW heating power, respectively. As shown, increasing the heating power would lead to more vapor generation inside the vapor chamber and causes higher pressure and temperature, since the eductor capacity to suck the vapor out of the chamber decreases. The suction capacity of the eductor is highly dependent on its size and the motive fluid flow rate. Increasing the rate of vaporization i.e. increasing the heating power, will cause the eductor to lose its effect after some point. Figure 15 indicates that the selected closed eductor system is capable of keeping the temperature and pressure of the chamber below 30 °C and 5 kPa, with the heating power of roughly 25 kW, which is the desired condition for the proposed thermal desalination techniques.

Figure 16 shows the water vapor temperature at the eductor inlet (T_4 in Fig. 12a) and the motive water

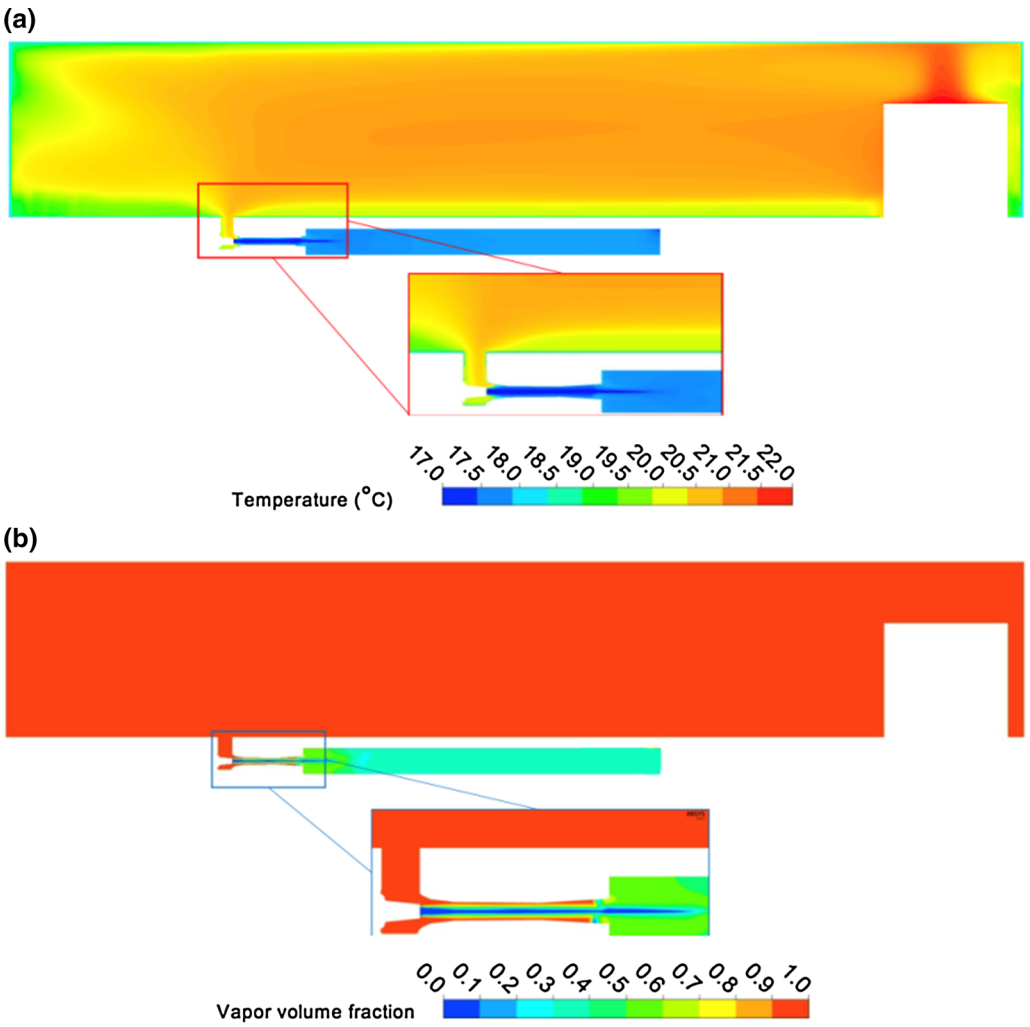

Fig. 11 (Color online) **a** Temperature, and **b** vapor volume fraction contours in the system with closed eductor and 4-in. ID mixing line

temperature at the mixing line outlet (T_5 in Fig. 12a) against different heating powers of 0, 7.7, 15.2 and 22.1 kW. The temperatures shown in Fig. 16 indicates that although the water vapor temperature at the eductor inlet increases from 14.2 to 23.8 °C when increasing the heating power from 0 to 22.1 kW, the motive water temperature at the mixing line outlet remains almost constant due to the higher mass flow rate of the motive water. The reason is that the mass flow rate of the motive water required to create the partial vacuum condition inside the chamber, is relatively more than the mass of vapor sucked into the eductor, which cause the temperature of mixture at the end of mixing line to remain unaffected by the heater power. Further data from this experiment are summarized in Table 4.

To reduce the energy consumption of the system, the motive water flow rate has to be minimized while maintaining the temperature and pressure of the chamber below the design threshold, which is 30 °C and 5 kPa for the proposed system. Figure 17 shows the amount of fresh water generation with respect to heating power input and motive water flow rate. As expected, fresh water generation increase approximately linearly with heating power. The critical motive water flow rate increases with heating power which drives the rate of vapor generation. Figure 17b shows that fresh water generation increases in a quasi-linear fashion with heating power input as long as the motive water flow rate is sufficiently high to create the desired vacuum condition inside the evaporation chamber, and shows an asymptotic behaviour. Thereafter increasing the motive water flow rate beyond a critical value would not affect the pressure condition in the evaporation chamber any further and as such, the fresh water generation approaches a limit.

Figure 18 shows the chamber temperature and pressure against the motive water flow rate. Heating power input to the steam generator is kept constant at 22.1 kW. The chamber temperature and the pressure decrease from

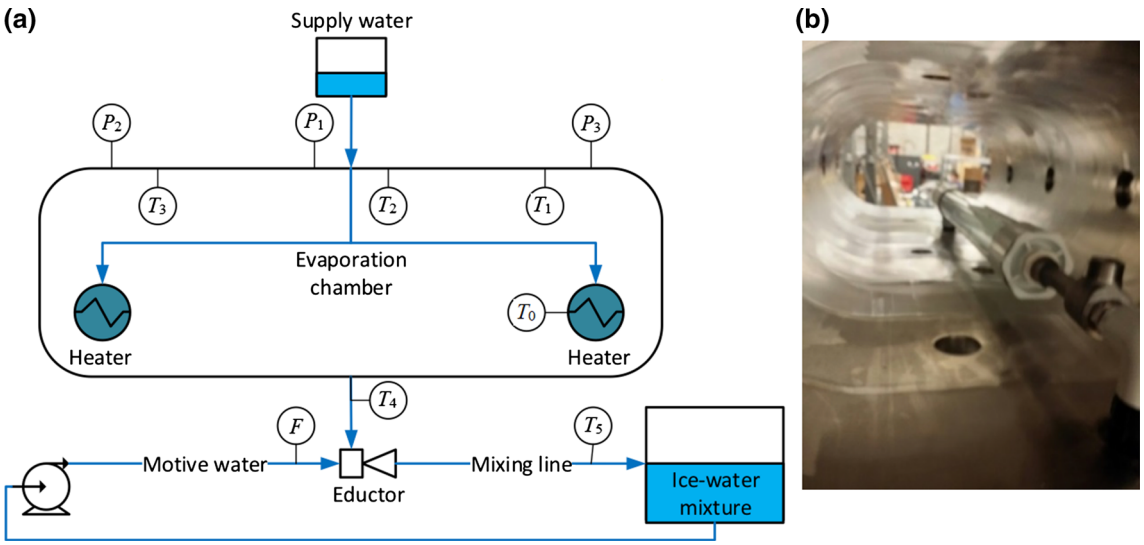

Fig. 12 (Color online) **a** Schematic of the testbed with closed eductor with the location of sensors; F: flow meter, P_1–P_3: pressure transducer, T_0: vapor temperature, T_1–T_3: evaporation chamber temperature, T_4: temperature at the eductor inlet, and T_5: mixture temperature at the mixing line outlet. **b** Inside view of the evaporation chamber with open eductor

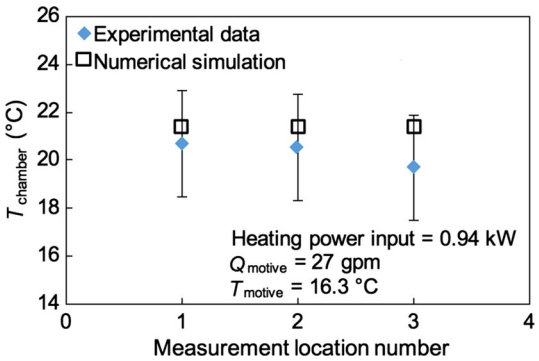

Fig. 13 (Color online) Comparison between experimental and predicted water vapor temperatures for closed eductor system at location 1–3 (cf. Fig. 12a)

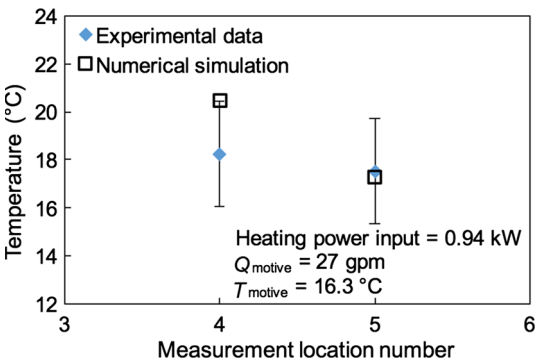

Fig. 14 (Color online) Comparison between the measured and predicted water vapor temperature at the eductor inlet and mixing line outlet

26.3 °C and 2.81 kPa at motive water flow rate of 137 gpm, to 25.9 °C and 2.71 kPa at motive water flow rate of 178 gpm, respectively. As expected, before reaching its geometrical limits, which is dictated by the size here, increasing the motive water flow rate of the eductor can cause higher suction effects at the inlet and decrease the pressure and temperature of the evaporation chamber. Figure 18 indicates the closed eductor can maintain the temperature and pressure of the chamber below 30 °C and 5 kPa while the chilled water flow rate is reduced from 178 to 137 gpm (23 %).

Figure 19 shows the water vapor temperature at the eductor inlet (T_4 in Fig. 12a) and the mixture temperature at the mixing line outlet (T_5 in Fig. 12a) against chilled water flow rates of 178 and 137 gpm. The vapor temperature at the eductor inlet does not change significantly (<0.5 °C) by increasing the motive water flow rate from 137 to 178 gpm, and hence a motive water flow rate of 137 gpm could be used for the eductor. As explained before, due to the already high ratio of motive water to vapor mass flow rate, the mixture temperature at the mixing line outlet is not affected much by the flow rate of the motive water. Further data are summarized in Table 5.

5 Conclusions

The feasibility of an educator assisted passive solar desalination system was investigated using a detailed 3D computational analysis complemented by experiments. In

Table 3 Comparison between the experimental and CFD simulation data at heating power input of 1 kW to the steam generator

Parameter	$P_{chamber}$ (kPa)	T_{motive} (°C)	T_{steam} (°C)	T_1 (°C)	T_2 (°C)	T_3 (°C)	T_4 (°C)	T_5 (°C)
Experimental data	2.2	16.3	22.2	20.7	20.5	19.7	18.2	17.5
Numerical data	3.2	17.0	22.2	21.4	21.4	21.4	20.5	17.3

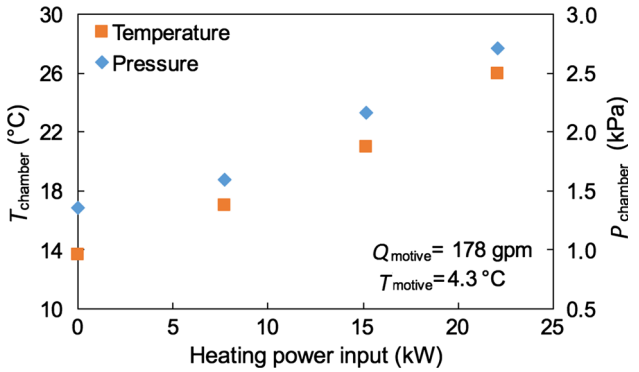

Fig. 15 (Color online) Measured evaporation chamber temperature and pressure versus heating power input

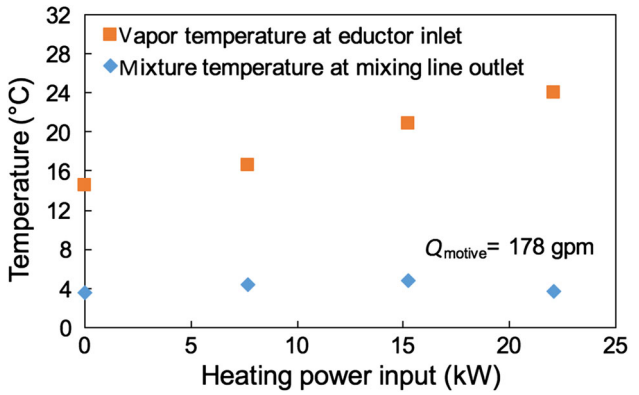

Fig. 16 (Color online) Variation of water vapor temperature with heating power input to the steam generator: (square) at the inlet of the eductor (T_4 in Fig. 12a); (losange) chilled water temperature at the outlet of the mixing line (T_5 in Fig. 12a)

Table 4 Experimental data measured in the evaporation chamber equipped with closed eductor and the chilled water flow rate of 178 gpm

Power (kW)	$P_{chamber}$ (kPa)	T_{motive} (°C)	T_{steam} (°C)	T_1 (°C)	T_2 (°C)	T_3 (°C)	T_4 (°C)	T_5 (°C)
0	1.4	4.0	13.7	14.8	14.7	14.3	14.2	3.5
7.7	1.6	4.7	17.0	16.6	16.6	16.7	16.5	4.3
15.2	2.2	4.9	21.0	20.9	20.8	20.8	20.6	4.7
22.1	2.7	3.7	26.0	24.0	24.0	24.0	23.9	3.7

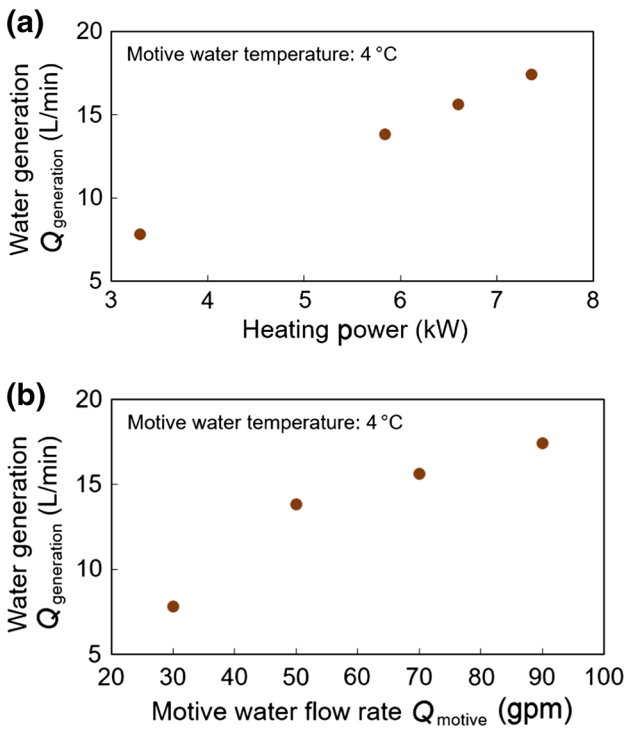

Fig. 17 (Color online) Variation of fresh water generation with heating power input to the steam generator (**a**), and chilled water mixture flow rate (**b**)

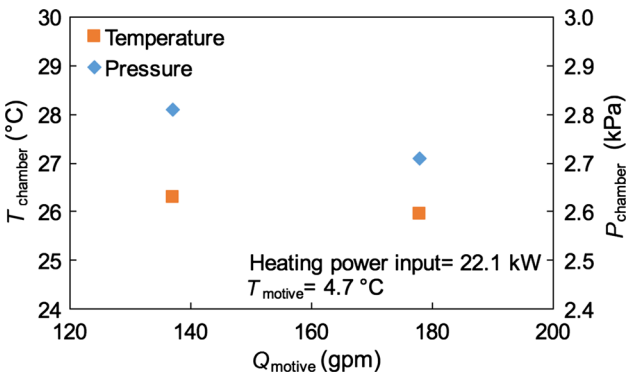

Fig. 18 (Color online) Experimental data collected in the evaporator chamber: steam generator temperature and chamber pressure versus chilled water mixture flow rate

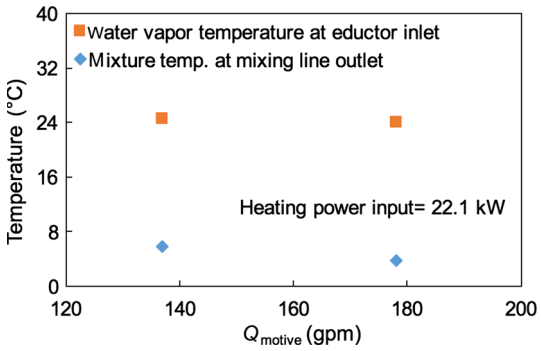

Fig. 19 (Color online) Water vapor temperature at the eductor inlet (T_4 in Fig. 12a) and the motive water temperature at the mixing line outlet (T_5 in Fig. 12a) versus motive water flow rate

Table 5 Experimental date measured in the evaporation chamber equipped with closed eductor and the heating power input of 22.1 kW

Q_{motive} (gpm)	$P_{chamber}$ (kPa)	T_{motive} (°C)	T_{steam} (°C)	T_1 (°C)	T_2 (°C)	T_3 (°C)	T_4 (°C)	T_5 (°C)
137	2.8	5.8	26.3	24.6	24.5	24.6	24.3	5.9
178	2.7	3.7	26.0	24.0	24.0	24.0	23.9	3.7

the proposed system, an educator is used instead of a vacuum pump to reduce the process pressure. The study focused in particular on the ability of the new design to lower the required evaporation temperature and thereby reduce the energy intensity of the process. Two configurations were investigated and a detailed analysis of the thermofluid processes was performed. The open educator systems did not yield sufficient condensation in the mixing line. A configuration with a closed educator installed outside the evaporation chamber shows very promising performance. The proposed system can maintain the maximum temperature and pressure in the evaporation chamber below desirable temperature and pressure thresholds (30 °C and 5 kPa). The analysis and experimental data also show it is possible to further reduce energy requirements by reducing the motive water flow rates. Based on the overall agreement achieved between the CFD predictions and the measurements, further study and optimization of the educator assisted desalination systems, including scaling, will be undertaken in future work.

Acknowledgments Funding and technical support for this work was provided in part by the Deanship of Scientific Research, King Abdulaziz University, Jeddah, under Grant No. (1-135-36-HiCi). The authors would also like to thank Dr. Amir Sharafian for his contributions to this study.

Conflict of interest The authors declare that they have no conflict of interest.

References

1. UN Water (2014) The United Nations world water development report 2014: water and energy. UNESCO, Paris
2. Bogardi JJ, Dudgeon D, Lawford R et al (2012) Water security for a planet under pressure: interconnected challenges of a changing world call for sustainable solutions. Curr Opin Environ Sustain 4:35–43
3. Gössling S, Peeters P, Hall CM et al (2012) Tourism and water use: supply, demand, and security. An international review. Tour Manag 33:1–15
4. Kalogirou SA (2005) Seawater desalination using renewable energy sources. Prog Energy Combust Sci 31:242–281
5. Burn S, Hoang M, Zarzo D et al (2015) Desalination techniques—a review of the opportunities for desalination in agriculture. Desalination 364:2–16
6. Mahmoudi H, Spahis N, Abdul-Wahab SA et al (2010) Improving the performance of a seawater Greenhouse desalination system by assessment of simulation models for different condensers. Renew Sustain Energy Rev 14:2182–2188
7. Anderson MA, Cudero AL, Palma J (2010) Capacitive deionization as an electrochemical means of saving energy and delivering clean water. Comparison to present desalination practices: will it compete? Electrochim Acta 55:3845–3856
8. Wang LK, Chen JP, Hung YT et al (2011) Membrane and desalination technology. In: Handbook of environmental engineering, vol 13. Humana Press, New York
9. Cipollina A, Micale G, Rizzuti L (2009) Seawater desalination: conventional and renewable energy processes. Springer, Berlin
10. AlMarzooqi FA, Al Ghaferi AA, Saadat I et al (2014) Application of capacitive deionisation in water desalination: a review. Desalination 342:3–15
11. Bergen A, Djilali N, Fyles TM et al (2003) An experimental assessment of centrifugal membrane separation using spiral wound RO membrane elements. Desalination 154:225–232
12. Ghaffour N, Missimer TM, Amy GL (2013) Technical review and evaluation of the economics of water desalination: current and future challenges for better water supply sustainability. Desalination 309:197–207
13. Semiat R (2008) Critical review energy issues in desalination processes. Environ Sci Technol 42:8193–8201
14. Borsani R, Rebagliati S (2005) Fundamentals and costing of MSF desalination plants and comparison with other technologies. Desalination 182:29–37
15. Li C, Goswami Y, Stefanakos E (2013) Solar assisted sea water desalination: a review. Renew Sustain Energy Rev 19:136–163
16. Szacsvay T, Hofer-Noser P, Posnansky M (1999) Technical and economic aspects of small-scale solar-pond-powered seawater desalination systems. Desalination 122:185–193
17. Agha KR (2009) The thermal characteristics and economic analysis of a solar pond coupled low temperature multi stage desalination plant. Sol Energy 83:501–510
18. Al Hawaj O, Darwish MA (1994) A solar pond assisted multi-effect desalting system. Desalination 99:119–135
19. Garmana MA, Muntasserb MA (2008) Sizing and thermal study of salinity gradient solar ponds connecting with the MED desalination unit. Desalination 222:689–695
20. Tahri K (2001) The prospects of fresh water supply for Tan Tan City from non-conventional water resources. Desalination 135:43–50
21. El-Nashar AM (1993) An optimal design of a solar desalination plant. Desalination 93:597–614
22. El-Nashar AM (2000) Validating the performance simulation program "SOLDES" using data from an operating solar desalination plant. Desalination 130:235–253

23. Goosen MFA, Sablani SS, Paton C et al (2003) Solar energy desalination for arid coastal regions: development of a humidification-dehumidification seawater greenhouse. Sol Energy 75:413–419
24. Mahmoudi H, Abdul-Wahab SA, Goosen MF et al (2008) Weather data and analysis of hybrid photovoltaic–wind power generation systems adapted to a seawater greenhouse desalination unit designed for arid coastal countries. Desalination 222:119–127
25. Gude VG, Nirmalakhandan N (2009) Desalination at low temperatures and low pressures. Desalination 244:239–247
26. Kneass SL (1894) Practice and theory of the injector. Wiley, New York
27. Perry RH (2007) Perry's chemical engineers' handbook. McGraw Hill, New York
28. Power RB (1994) Steam jet ejectors for the process industries. McGraw-Hill, New York
29. Khaghani A, Date A, Akbarzadeh A (2013) Sustainable removal of non-condensable gases from geothermal waters. Renew Sustain Energy Rev 21:204–214
30. Reed RJR, Forrest IS (1986) Performance of a steam eductor in a pilot brewery. J Inst Brew 92:370–378
31. Antonio YM, Périlhon C, Descombes G et al (2012) Thermodynamic modelling of an ejector with compressible flow by a one-dimensional approach. Entropy 14:599–613
32. Rogdakis ED, Alexis GK (2000) Design and parametric investigation of an ejector in an air-conditioning system. Appl Therm Eng 20:213–226
33. El-Nashar AM (1984) Solar desalination using the vacuum freezing ejector absorption (VFEA) process. Desalination 49:293–319
34. Chen JZ, Li YF, Li GH (2011) A new method for desalination of seawater with steam-ejector refrigeration plant. Appl Mech Mater 94–96:273–279
35. Li C (2012) Innovative desalination systems using low-grade heat. Ph.D. Dissertation University of South Florida
36. Manninen M, Taivassalo V, Kallio S (1996) On the mixture model for multiphase flow. VTT Publications 288, Technical Research Centre of Finland
37. Schiller L, Naumann Z (1935) A drag coefficient correlation. VDI Zeitung 77:318–320
38. Hanjalic K, Kenjeres S (2008) Some developments in turbulence modeling for wind and environmental engineering. J Wind Eng Ind Aerodyn 96:1537–1570
39. Suksangpanomrung A, Djilali N, Moinat P (2000) Large eddy simulation of separated flow over a bluff plate. Int J Heat Fluid Flow 21:655–663
40. Lee WH (1979) A pressure iteration scheme for two-phase modeling. Technical Paper No. LA-UR-79-975, Los Alamos, NM
41. Celik IB, Ghia U, Roache P et al (2008) Procedure for estimation and reporting of uncertainty due to discretization in CFD applications. J Fluids Eng 130:078001